

A Tale of Two Metals: New Cerium Iron Borocarbide Intermetallics Grown from Rare-Earth/Transition Metal Eutectic Fluxes

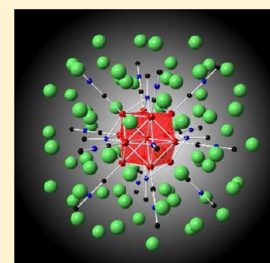
Patricia C. Tucker,[†] Jason Nyffeler,[†] Banghao Chen,[†] Andrew Ozarowski,[‡] Ryan Stillwell,[‡] and Susan E. Latturer^{*†}

[†]Department of Chemistry and Biochemistry, Florida State University, Tallahassee, Florida 32306, United States

[‡]National High Magnetic Field Laboratory, Florida State University, Tallahassee, Florida 32310, United States

S Supporting Information

ABSTRACT: $R_{33}Fe_{14-x}Al_{x+y}B_{25-y}C_{34}$ ($R = La$ or Ce ; $x \leq 0.9$; $y \leq 0.2$) and $R_{33}Fe_{13-x}Al_xB_{18}C_{34}$ ($R = Ce$ or Pr ; $x < 0.1$) were synthesized from reactions of iron with boron, carbon, and aluminum in R–T eutectic fluxes ($T = Fe, Co,$ or Ni). These phases crystallize in the cubic space group $Im\bar{3}m$ ($a = 14.617(1)$ Å, $Z = 2$, $R_1 = 0.0155$ for $Ce_{33}Fe_{13.1}Al_{1.1}B_{24.8}C_{34}$, and $a = 14.246(8)$ Å, $Z = 2$, $R_1 = 0.0142$ for $Ce_{33}Fe_{13}B_{18}C_{34}$). Their structures can be described as body-centered cubic arrays of large Fe_{13} or Fe_{14} clusters which are capped by borocarbide chains and surrounded by rare earth cations. The magnetic behavior of the cerium-containing analogs is complicated by the possibility of two valence states for cerium and possible presence of magnetic moments on the iron sites. Temperature-dependent magnetic susceptibility measurements and Mössbauer data show that the boron-centered Fe_{14} clusters in $Ce_{33}Fe_{14-x}Al_{x+y}B_{25-y}C_{34}$ are not magnetic. X-ray photoelectron spectroscopy data indicate that the cerium is trivalent at room temperature, but the temperature dependence of the resistivity and the magnetic susceptibility data suggest $Ce^{3+/4+}$ valence fluctuation beginning at 120 K. Bond length analysis and XPS studies of $Ce_{33}Fe_{13}B_{18}C_{34}$ indicate the cerium in this phase is tetravalent, and the observed magnetic ordering at $T_C = 180$ K is due to magnetic moments on the Fe_{13} clusters.



INTRODUCTION

Metal flux synthesis has proven to be a vital tool for the discovery and crystal growth of new solids. This synthesis technique allows for the solvation of refractory elements in low melting metal solvents; the low reaction temperatures afforded by this method can promote the growth of new intermetallic compounds with complex structures.¹ Expanding from single metal solvents to mixed fluxes comprised of two metals can allow for lowered solvent melting points through formation of eutectics; it also increases the number of reactants that are soluble and reactive in the flux. The use of mixed metal eutectic fluxes has aided the discovery of a broad range of new intermetallic phases and Zintl phase compounds such as $Ca_{21}Ni_2Zn_{36}$ (grown in Ca–Zn eutectic), $Co_7Zn_3Sn_8$ (grown in Zn–Sn eutectic), and $LiCa_2C_3H$ (grown in Ca–Li mixture).^{2–4} Our explorations of reactions in La–Ni eutectic flux (mp 517 °C) have yielded several new multinary intermetallics comprised of lanthanum, a transition metal, and one or more main group elements; examples include $La_{21}T_8M_7C_{12}$ ($T = Mn, Fe$; $M = Ge, Sn, Sb, Te, Bi$), $La_2Ni_{2-x}Ru_xAl$, and $La_{14}Sn(MnC_6)_3$.^{5–7}

Expanding on the La–Ni eutectic work, Ce–T and Pr–T ($T = Fe, Co, Ni$) eutectic fluxes are now being investigated as synthesis media for magnetic intermetallic materials. Phases containing both a paramagnetic rare earth and a transition metal may feature complex magnetic behavior as the moments on these atoms couple in various ways at different temperatures, as is seen for compounds such as $SmCo_5$ and $PrCo_2P_2$.^{8,9} Cerium-containing intermetallics can exhibit

particularly interesting phenomena due to the fact that the energy of the Ce 4f electron is often close to the Fermi level, leading to the possibility of two valence states (Ce^{3+} or Ce^{4+}) and variation in valence with temperature or pressure. This can result in mixed valence structures ($Ce_{23}Ru_7Cd_4$),¹⁰ valence fluctuation (Ce_2RuZn_4),¹¹ and heavy fermion behavior ($CeRhIn_5$).¹²

In this work, two structurally related cerium iron borocarbide intermetallics have been grown from Ce/T eutectic fluxes. Both structures feature several cerium sites surrounding clusters of iron capped with borocarbide chains. $Ce_{33}Fe_{13.1}Al_{1.1}B_{24.8}C_{34}$ exhibits cerium valence fluctuation; its boron-centered Fe_{14} clusters do not possess magnetic moments. $Ce_{33}Fe_{13}B_{18}C_{34}$ is comprised of tetravalent Ce ions (possibly the result of chemical pressure) and cuboctahedral Fe_{13} clusters which order ferromagnetically.

The Fe_{13} and Fe_{14} clusters are highly unusual structural building blocks. $R_{33}Fe_{14-x}Al_{x+y}B_{25-y}C_{34}$ ($R = La, Ce$) and $R_{33}Fe_{13-x}Al_xB_{18}C_{34}$ ($R = Ce, Pr$) occupy the relatively unexplored phase space between intermetallic compounds with isolated (and usually nonmagnetic) iron sites such as $La_{3.67}FeC_6$ and $ErFe_4Al_9Si_6$, and compounds with extended iron building blocks featuring strong magnetic moments, such as $R_6Fe_{14-x}Al_x$ and $Nd_2Fe_{14}B$.^{13–16} The variation in magnetic properties of the iron clusters in the title phases is due to different Fe–Fe distances and number of nearest neighbor iron

Received: April 8, 2012

Published: June 25, 2012

atoms, as well as the extent of aluminum substitution on iron sites. Tailoring magnetic properties by careful control of substitution in phases such as $\text{Nd}_2\text{Fe}_{14-x}\text{M}_x\text{B}$ and $\text{SmCo}_{5-x}\text{M}_x$ is a topic of widespread interest;¹⁶ studying this process in the smaller iron clusters available in these new Ce/Fe/B/C phases may shed light on how magnetic moments develop in hard magnetic materials.

EXPERIMENTAL PROCEDURE

Synthesis. Starting materials were stored and handled in an argon-filled drybox. Powders of the following elements were used in reactions: carbon black (Strem Chemicals 95–97%), boron (Strem Chemicals 95–97%), iron (Alfa Aesar 99%), manganese (Alfa Aesar 99%), aluminum (Alfa Aesar 99%), nickel (Alfa Aesar 99%), and iron-57 (Isoflex USA 96.63% enrichment). Iron-57 was used for the synthesis of an enriched sample of $\text{Ce}_{33}\text{Fe}_{14-x}\text{Al}_{x+y}\text{B}_{25-y}\text{C}_{34}$ for Mössbauer spectroscopy. R–T eutectics were either purchased (La–Ni, Alfa-Aesar; 67% La with mp 517 °C) or made by arc-melting appropriate amounts of rare earth and transition metals under argon. For instance, Ce–Co eutectic was made from cerium ingot (Alfa Aesar, 99.999%) and cobalt slug (Alfa Aesar 99.95%), by arc melting a 76:24% mole ratio of these elements (mp 424 °C)¹⁷ on a water-cooled copper hearth into a button that was turned over and remelted several times to ensure homogeneity of the flux material. Similarly, Ce–Fe eutectic was made from cerium ingot and iron slug (Alfa Aesar 99%) in a 83:17% mole ratio (mp 592 °C); Ce–Ni eutectic from cerium ingot and nickel slug (Alfa Aesar 99%) in a 78:22% mole ratio (mp 477 °C); Pr–Fe eutectic from praseodymium ingot (Alfa Aesar 99.9%) and Fe slug using a 79:21% mole ratio (mp 620 °C); Pr–Ni eutectic from praseodymium ingot and nickel slug in a 81:19% mole ratio (mp 460 °C).¹⁷ These brittle eutectic ingots were fragmented into approximately 1 mm³ size pieces; 1.5 g of eutectic were used per reaction.

Reactions in the various R–T eutectics were prepared by sandwiching C, B, Ni, Al, and either Mn, Fe, or Fe-57 (combined in a 1:1:1:1:1 mmol ratio) between layers of R–T eutectic, with more flux on the top layer than the bottom one. Reactants and flux were loaded into either alumina or steel crucibles (ca. 8 mm inside diameter, 30 mm length) and a second alumina crucible filled with Fiberfrax was inverted and placed on top of the reaction crucible to act as a filter during centrifugation. These crucible configurations were placed into silica tubes, which were flame-sealed under a vacuum of 10^{−2} Torr. The ampules were then heated to 950 °C in 3 h, held at this temperature for 12 h, and then cooled to 850 °C in 10 h. The reaction mixtures were subsequently annealed for 48 h at 850 °C and then cooled to 600 °C in 84 h. At 600 °C the ampules were removed from the furnace, quickly inverted, and placed into a centrifuge to decant the molten flux. (Reactions in the higher-melting Ce–Fe eutectic were instead cooled to 700 °C and centrifuged.) Products from these reactions were stored in an argon-filled drybox in order to prevent oxidation.

Stoichiometric syntheses of $\text{R}_{33}\text{Fe}_{14-x}\text{Al}_{x+y}\text{B}_{25-y}\text{C}_{34}$ and $\text{R}_{33}\text{Fe}_{13-x}\text{Al}_x\text{B}_{18}\text{C}_{34}$ were attempted by combining elemental forms of R (R = La, Ce, Pr, Nd, Sm), Fe, B, and C in appropriate ratios (for instance, a 6.6:2.8:5.0:6.8 mmol ratio for $\text{R}_{33}\text{Fe}_{14}\text{B}_{25}\text{C}_{34}$) in an alumina crucible. These reactions were prepared in an argon-filled drybox, and the crucible was placed in a fused silica tube and sealed under a vacuum of 10^{−2} Torr. The ampule was then heated to 950 °C in 3 h, held at this temperature for 168 h, and then cooled to 25 °C in 3 h. Products were stored in an argon-filled drybox to prevent oxidation of the powders.

Elemental Analysis. Elemental analysis was performed on all samples using a JEOL S900 scanning electron microscope (SEM) with energy-dispersive X-ray spectroscopy (EDXS) capabilities. Flux-grown crystals from each reaction were affixed to an aluminum SEM puck using carbon tape, fractured to expose inner regions, and positioned so that flat faces were perpendicular to the electron beam. Samples were analyzed using a 30 kV accelerating voltage and an accumulation time of 60s. A rare earth:iron ratio of 7:3 was consistently found for $\text{R}_{33}\text{Fe}_{14-x}\text{Al}_{x+y}\text{B}_{25-y}\text{C}_{34}$ and $\text{R}_{33}\text{Fe}_{13-x}\text{Al}_x\text{B}_{18}\text{C}_{34}$ phases; nickel content

was negligible (below 1 mol %). Small amounts of aluminum (1–2%) were indicated in the $\text{R}_{33}\text{Fe}_{14-x}\text{Al}_{x+y}\text{B}_{25-y}\text{C}_{34}$ and $\text{PR}_{33}\text{Fe}_{13-x}\text{Al}_x\text{B}_{18}\text{C}_{34}$ crystals. No aluminum was indicated in the data for $\text{Ce}_{33}\text{Fe}_{13}\text{B}_{18}\text{C}_{34}$ samples. The carbon and boron content was not able to be determined due to the limitation of the EDXS in detecting the characteristic X-rays of light elements. Quantitative determination of the carbon content of $\text{Ce}_{33}\text{Fe}_{14-x}\text{Al}_{x+y}\text{B}_{25-y}\text{C}_{34}$ was carried out by combustion analysis (Atlantic Microlabs). A 60 mg sample of $\text{Ce}_{33}\text{Fe}_{14-x}\text{Al}_{x+y}\text{B}_{25-y}\text{C}_{34}$ crystals was sent for analysis to determine the amount of C present. Two runs of 30 mg each were performed, yielding carbon mass percents of 5.46% and 5.57%.

X-ray Photoelectron Spectroscopy. Analyses of cerium valence and light elements were performed on $\text{Ce}_{33}\text{Fe}_{14-x}\text{Al}_{x+y}\text{B}_{25-y}\text{C}_{34}$ and $\text{Ce}_{33}\text{Fe}_{13}\text{B}_{18}\text{C}_{34}$ samples previously screened by EDS, using a Physical Electronics PHI 5100 series XPS with a nonmonochromated dual anode (Al and Mg) source having a single channel hemispherical energy analyzer. Large single crystals were affixed to a carbon coated sample puck using carbon tape. The Al X-ray source was used to study higher binding energies. To remove surface oxides and flux residue, samples were sputtered by Ar⁺ ions as the sample stage was rotated. Spectra were taken after every 5–10 min of sputtering to monitor the disappearance of surface oxide peaks and appearance of new species. Once no more changes in spectra were observed, sputtering was stopped.

X-ray Diffraction. Selected single crystals of each phase were mounted on cryo loops using paratone oil. X-ray diffraction data were collected at 150 K on a Bruker SMART APEX2 CCD diffractometer equipped with a Mo-target X-ray tube ($\lambda = 0.71073$). The data sets were recorded as ω scans at 0.3° step width and integrated with the Bruker SAINT software. Data were corrected for absorption effects using the multiscan method (SADABS).¹⁸ The structures were refined in the centrosymmetric space group $Im\bar{3}m$ (space group number 229) by full matrix least-squares procedures on $|F^2|$ using the SHELX-97 software package.¹⁹ The rare earth and iron atoms were located using direct methods, and the light atoms were indicated by residual electron density peaks of 5–10 e[−]/Å³ in the difference Fourier maps. Light atom sites were initially assigned as boron. Allowing their occupancy to vary did not distinguish boron from carbon (the scattering factors of these elements are too similar), so assignments of these sites were based on comparison of observed bond lengths to those in other rare earth borocarbides (see discussion). During final refinement cycles occupancies of each site were allowed to vary to identify possible site mixing. Unit cell parameters and crystallographic data collection information are found in Tables 1 and 2; atomic coordinates and displacement parameters are found in the Supporting Information.

Table 1. $\text{R}_{33}\text{Fe}_{14-x}\text{Al}_{x+y}\text{B}_{25-y}\text{C}_{34}$ and $\text{R}_{33}\text{Fe}_{13-x}\text{Al}_x\text{B}_{18}\text{C}_{34}$ Phases Grown from R/T Fluxes and Parameters from Single Crystal Diffraction Data Refinements

compound	unit cell (Å)	r-factor (R_1/wR_2)
$\text{La}_{33}\text{Fe}_{13.9(1)}\text{Al}_{0.3(1)}\text{B}_{24.8(1)}\text{C}_{34}$	14.8560(8)	0.0184/0.0326
$\text{Ce}_{33}\text{Fe}_{13.1(1)}\text{Al}_{1.1(1)}\text{B}_{24.8(1)}\text{C}_{34}$	14.617(1)	0.0155/0.0350
$\text{Ce}_{33}\text{Mn}_{14}\text{Al}_{0.1(1)}\text{B}_{24.9(1)}\text{C}_{34}$	14.615(1)	0.0155/0.0345
$\text{Ce}_{33}\text{Fe}_{13}\text{B}_{18}\text{C}_{34}$	14.246(8)	0.0142/0.0285
$\text{Pr}_{33}\text{Fe}_{12.9(1)}\text{Al}_{0.1(1)}\text{B}_{18}\text{C}_{34}$	14.3881(9)	0.0127/0.0271

Powder X-ray diffraction data were collected using a Rigaku Ultima III diffractometer with a Cu radiation source and a CCD detector. Samples were ground with a small amount of silicon to act as an internal standard. Experimental powder patterns were compared to calculated patterns based on single crystal data to confirm the presence of the desired phase. Unit cell parameters were determined by using the accompanying refinement software contained in the JADE software ($a = 14.850(9)$, $14.581(4)$, and $14.390(1)$ Å for $\text{La}_{33}\text{Fe}_{14-x}\text{Al}_{x+y}\text{B}_{25-y}\text{C}_{34}$, $\text{Ce}_{33}\text{Fe}_{14-x}\text{Al}_{x+y}\text{B}_{25-y}\text{C}_{34}$, and $\text{PR}_{33}\text{Fe}_{13-x}\text{Al}_x\text{B}_{18}\text{C}_{34}$, respectively). Byproducts were identified by comparison with patterns in the JADE software database.

Table 2. Crystallographic Data Collection Parameters for Selected R/T/B/C Phases

	Ce ₃₃ Fe _{13.1} Al _{1.1} B _{24.8} C ₃₄	Ce ₃₃ Fe ₁₃ B ₁₈ C ₃₄	Pr ₃₃ Fe _{12.9} Al _{0.1} B ₁₈ C ₃₄
formula weight (g/mol)	6055.58	5952.93	5977.8
crystal system		cubic	
space group		<i>Im</i> $\bar{3}m$	
<i>a</i> (Å)	14.617(1)	14.246(8)	14.3881(9)
<i>Z</i>	2	2	2
volume	3123.2(4)	2891(3)	2978.6(3)
density, calc (g/cm ³)	6.44	6.84	6.67
radiation		Mo <i>K</i> α	
temperature (K)		150	
index ranges	$-18 \leq h \leq 18$ $-19 \leq k \leq 19$ $-19 \leq l \leq 19$	$-18 \leq h \leq 18$ $-18 \leq k \leq 18$ $-18 \leq l \leq 18$	$-18 \leq h \leq 18$ $-19 \leq k \leq 19$ $-18 \leq l \leq 18$
theta range (deg)	1.97–28.21	2.02–28.25	2.00–28.20
reflections collected	17 445	15 157	16 857
unique data/parameters	419/42	388/36	402/38
μ (mm ⁻¹)	26.41	28.51	29.44
<i>R</i> ₁ / <i>wR</i> ₂	0.0155/0.0350	0.0142/0.0285	0.0127/0.0271
<i>R</i> ₁ / <i>wR</i> ₂ (all data)	0.0186/0.0354	0.0143/0.0285	0.0137/0.0273
residual peak/hole (e ⁻ /Å ³)	1.015/–1.350	0.826/–0.679	0.834/–1.430

Magnetic Susceptibility. Magnetic measurements were carried out with a Quantum Design MPMS SQUID magnetometer. For each sample, a large single crystal was weighed and then placed at the 3 cm mark of a 12 cm piece of kapton tape. The kapton tape was folded in half to enclose the crystal. Then the piece of tape containing the crystal was placed in a plastic straw and then loaded into the magnetometer. Both field-cooled (FC) and zero-field cooled (ZFC) measurements were collected at an applied field of 100 Oe with a temperature range of 2–300 K, and field dependence data were collected from 0 to 70 000 Oe at several temperatures.

Mössbauer Spectroscopy. Mössbauer Spectroscopy measurements on Ce₃₃Fe_{14-x}Al_{x+y}B_{25-y}C₃₄ grown using enriched ⁵⁷Fe were carried out using a SEE Co. Mössbauer spectrometer installed with a gamma source, ⁵⁷Co embedded in Rh matrix, with an initial intensity of 110 milliCurie manufactured by Isotope. Temperature was controlled with a Janis helium cryostat. Measurements were performed at ± 3 mm/s at 5.5, 78, 150, and 294 K, and at ± 10 mm/s at 5.5 and 78 K.

Solid State NMR Spectroscopy. ¹¹B MAS NMR spectra of Ce₃₃Fe_{14-x}Al_{x+y}B_{25-y}C₃₄ were collected on a Varian Unity Inova 500 MHz wide-bore NMR spectrometer equipped with a three channel MAS probe. The Larmor frequency of ¹¹B was 160.538 MHz. Single crystals of Ce₃₃Fe_{14-x}Al_{x+y}B_{25-y}C₃₄ were ground with NaCl in a drybox (2:1 sample to NaCl by mass) to facilitate spinning of the sample in the magnetic field; the mixture was packed into a 4 mm zirconia rotor sealed with airtight screw caps. A typical small angle pulse (less than 15°) was applied to ensure quantitative spectra with a recycle delay of 5 s. Data were collected at 25 °C, and a 14 kHz spin rate was used. A total of 14 920 scans were collected for the NMR spectrum. The spectra were referenced to solid NaBH₄ at –42.16 ppm (with respect to BF₃OEt₂ at 0 ppm). Attempts were made to obtain ¹³C MAS NMR data, but no resonances were observed.

Resistivity. Resistivity measurements were conducted on Ce₃₃Fe_{14-x}Al_{x+y}B_{25-y}C₃₄ by a conventional four-point *dc* method on a Physical Property Measurement System (PPMS) by Quantum Design. A crystal (size: 1 mm \times 1 mm \times 1 mm) was mounted on the sample holder of a ⁴He probe with a small amount of glue and connected to the electrodes of the sample holder with 0.001 in. diameter gold wires using silver paint. Measurements were carried out from 1.8 to 300 K, using an applied excitation current of 3 mA.

RESULTS AND DISCUSSION

All of the binary alloy phase diagrams of early rare earth elements (R = La, Ce, Pr, Nd) combined with late first row

transition metals (T = Fe, Co, Ni, Cu) contain a low-melting eutectic in the rare-earth rich region.¹⁷ These eutectic melts have proven to be excellent solvents for iron, carbon, and most other elements, leading to formation of many new R/Fe/C/X phases. A recent review of known ternary R/T/C carbides classified such compounds into two groups: carbometallates (such as La_{3.67}FeC₆, featuring isolated transition metal atoms surrounded by carbon), or transition metal-rich carbides (such as Nd₂Fe₁₇C_{3-x}, featuring extensive Fe–Fe bonding).²⁰ However, several new phases have recently been discovered which fit between these classifications. Compounds such as La₂₁Fe₈Sn₇C₁₂ (grown in La/Ni flux),⁵ Dy₁₅Fe₈C₂₅,²¹ and the title phases R₃₃Fe_{14-x}Al_{x+y}B_{25-y}C₃₄ (R = La, Ce) and R₃₃Fe_{13-x}Al_xB₁₈C₃₄ (R = Ce, Pr) feature iron clusters of 4–14 atoms capped around the edges by carbon and/or boron. The intermediate size of these iron building blocks can lead to complex magnetic behavior. This complexity is furthered in the cerium iron borocarbide title phases due to the variable valency of cerium.

Synthesis. R₃₃Fe_{14-x}Al_{x+y}B_{25-y}C₃₄ (R = La, Ce) and R₃₃Fe_{13-x}Al_xB₁₈C₃₄ (R = Ce, Pr) grow from various R–T eutectic fluxes as large silver faceted spheroids up to 1–2 mm in diameter; see Figure 1. A manganese analog of one of the structures, Ce₃₃Mn₁₄Al_{0.1}B_{24.9}C₃₄, can also be synthesized. The compounds degrade slowly in air (over several days) and react rapidly with water. While product can be obtained from all the fluxes that were investigated, the highest yields were found for reactions in Ce–Co eutectic for Ce₃₃Fe_{14-x}Al_{x+y}B_{25-y}C₃₄ (70% yield based on carbon) and Pr–Ni flux for Pr₃₃Fe_{13-x}Al_xB₁₈C₃₄ (40% yield based on carbon; yield was significantly lower in Pr–Co). Yield increased with the addition of C and B, up to 1.2 mmol of each element added. Beyond this amount, unreacted C and B were observed in the centrifuged ampules, indicating a possible solubility limit. The Ce–Co and Ce–Ni fluxes are more convenient to use compared to the higher melting Ce–Fe eutectic, although they present the risk of cobalt or nickel incorporation into products. These elements were not observed in the EDS analyses of Ce₃₃Fe_{14-x}Al_{x+y}B_{25-y}C₃₄, but trace amounts of cobalt were detected in the manganese analog Ce₃₃Mn₁₄Al_{0.1}B_{24.9}C₃₄ grown from reactions in Ce–Co flux.

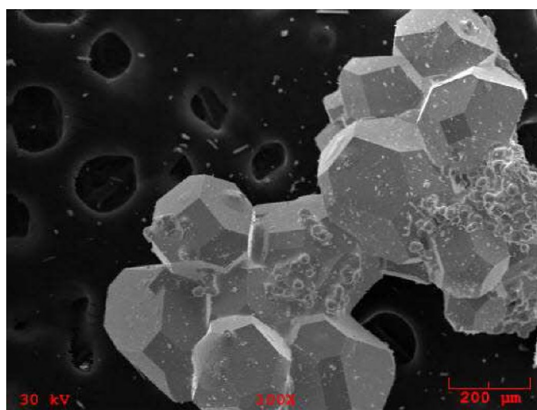


Figure 1. SEM image of crystals of $\text{Ce}_{33}\text{Fe}_{13.1}\text{Al}_{1.1}\text{B}_{24.8}\text{C}_{34}$ grown from Ce/Fe flux, displaying truncated octahedral growth habit.

This parallels what has been observed in previous reactions in La/Ni flux. For instance, in La/Ni flux syntheses of $\text{La}_6\text{T}_{14-x}\text{Al}_x$ reactions with $\text{T} = \text{Fe}$ yield $\text{La}_6\text{Fe}_{14-x}\text{Al}_x$ with no nickel incorporated; if $\text{T} = \text{Mn}$ is used instead, the $\text{La}_6\text{Mn}_{14-x}\text{Al}_x$ products do show doping of small amounts of nickel on some of the manganese sites.²² The reactivity of transition metals in these R/T eutectics—whether as added reactants or as components of the flux eutectic—appears to be $\text{Fe} > \text{Mn} \gg \text{Co}, \text{Ni}$.

The synthesis of the title phases is complicated by the fact that additional elements (Al and Ni) must be present in the flux to aid in their growth. A series of reactions were carried out to determine which elements were necessary for product formation. Reactions that did not contain both Ni and Al yielded predominantly pseudobinary phases such as $\text{Ce-Fe}_{2-x}\text{Co}_x$. Incorporation of trace amounts of aluminum may be required to stabilize the structures. This is also seen for phases such as $\text{LaFe}_{13-x}\text{Al}_x$ and $\text{La}_6\text{Fe}_{14-x}\text{Al}_x$; the binaries LaFe_{13} and $\text{La}_6\text{Fe}_{13}$ are not known.^{22,23} EDS analyses and structural refinement of single crystal XRD data for several “ $\text{R}_{33}\text{Fe}_{14}\text{B}_{25}\text{C}_{34}$ ” crystals consistently indicates substitution of Al on the Fe2 site and the B3 site, resulting in a stoichiometry of $\text{R}_{33}\text{Fe}_{14-x}\text{Al}_{x+y}\text{B}_{25-y}\text{C}_{34}$ (see Table 1). These phases were initially grown in alumina crucibles without Al reactant; the strongly reducing flux reacted with the crucible, adding aluminum metal to the reaction. When aluminum was deliberately added to subsequent reactions, the yield increased drastically. A very small amount of aluminum substitution is also seen in $\text{Pr}_{33}\text{Fe}_{13-x}\text{Al}_xB_{18}\text{C}_{34}$ ($x \approx 0.1$), but is not seen for the $\text{Ce}_{33}\text{Fe}_{13}\text{B}_{18}\text{C}_{34}$ analog.

Nickel does not appear to be incorporated into the products at all, so its role in the reaction may be to aid in solubilizing the boron reactant or to catalyze or nucleate the crystal growth of the phase. Similar behavior was observed for the gallium flux syntheses of $\text{Yb}_3\text{Ga}_7\text{Ge}_3$ and $\beta\text{-SiB}_3$, which require the presence of Pd and Cu, respectively.^{24,25} Reactions that did not include Ni resulted in a very small yield of product and unreacted boron. Attempts at using copper or other elements instead of nickel resulted in unreacted boron and crystals of $\text{CeFe}_{2-x}\text{Co}_x$ instead of the title phases. Despite the complexity of the synthesis, several analogs of each structure can be obtained reproducibly.

The identity of the rare earth determines whether $\text{R}_{33}\text{Fe}_{14-x}\text{Al}_{x+y}\text{B}_{25-y}\text{C}_{34}$ or $\text{R}_{33}\text{Fe}_{13-x}\text{Al}_xB_{18}\text{C}_{34}$ is formed, with larger La^{3+} ions producing the former structure, and smaller

Pr^{3+} ions yielding the latter. This is confirmed in both flux and stoichiometric synthesis. $\text{La}_{33}\text{Fe}_{14-x}\text{Al}_{x+y}\text{B}_{25-y}\text{C}_{34}$ is formed from either La/T flux reactions (as crystals) or as silver powder from stoichiometric combination of the elements. $\text{Pr}_{33}\text{Fe}_{13-x}\text{Al}_xB_{18}\text{C}_{34}$ is likewise isolated as crystals from Pr/T fluxes or as silver powder in stoichiometric reactions. Cerium ions can form both structures. For Ce flux reactions, the formation of either $\text{Ce}_{33}\text{Fe}_{14-x}\text{Al}_{x+y}\text{B}_{25-y}\text{C}_{34}$ or $\text{Ce}_{33}\text{Fe}_{13}\text{B}_{18}\text{C}_{34}$ is determined by the crucible used for synthesis. For reactions carried out in alumina crucibles, $\text{Ce}_{33}\text{Fe}_{14-x}\text{Al}_{x+y}\text{B}_{25-y}\text{C}_{34}$ is formed, possibly induced by leaching of trace Al from the crucible. Reactions carried out in steel crucibles produce $\text{Ce}_{33}\text{Fe}_{13}\text{B}_{18}\text{C}_{34}$ instead. Trace elements in the steel may promote the formation of this structure. Attempts at stoichiometric synthesis of the cerium phases produce only the $\text{Ce}_{33}\text{Fe}_{14-x}\text{Al}_{x+y}\text{B}_{25-y}\text{C}_{34}$ phase. The powder pattern matches that calculated from the single crystal data for this structure (Figure S1, Supporting Information). The amount of Al incorporation was unable to be determined because no single crystals were obtained, although trace amounts of Al were indicated in the EDS analysis of the powder. Flux reactions and stoichiometric syntheses using Nd and Sm did not form either $\text{R}_{33}\text{Fe}_{14-x}\text{Al}_{x+y}\text{B}_{25-y}\text{C}_{34}$ or $\text{R}_{33}\text{Fe}_{13-x}\text{Al}_xB_{18}\text{C}_{34}$ phases; these elements are too small to occupy the rare earth sites in these structures.

Light elements such as boron and carbon cannot be analyzed by SEM-EDXS; large crystals of $\text{Ce}_{33}\text{Fe}_{14-x}\text{Al}_{x+y}\text{B}_{25-y}\text{C}_{34}$ were therefore studied using XPS to determine whether or not these elements were present. Ar^+ ion sputtering was used to remove surface species from samples before XPS measurement. No boron peaks were observed before sputtering, possibly indicating coating of the crystals by traces of flux or surface enrichment by other elements. After sputtering, a peak appears at 196 eV, which is in the expected B 1s binding energy region.²⁶ The presence of carbon was also confirmed by the XPS data with the C 1s binding energy of 284 eV similar to that of other carbides such as Fe_3C (283.9 eV), SiC (283.8 eV), and BaC_2 (283.5 eV).²⁶ Carbon content was quantified by combustion analysis on samples of $\text{Ce}_{33}\text{Fe}_{14-x}\text{Al}_{x+y}\text{B}_{25-y}\text{C}_{34}$ (Atlantic Microlabs), which indicated 5.5% carbon by mass. This is lower than the 6.7% value expected from the stoichiometry, which may be due to flux coating of the samples, or oxidation during handling.

Structure of $\text{R}_{33}\text{M}_{14-x}\text{Al}_{x+y}\text{B}_{25-y}\text{C}_{34}$ ($\text{R} = \text{La}, \text{Ce}; \text{M} = \text{Fe}, \text{Mn}$). This structure crystallizes in the cubic space group $Im\bar{3}m$ with unit cell parameters decreasing with the size of the rare earth (see Table 1). The structure can be viewed as a *bcc* packing of borocarbide-capped Fe_{14}B clusters as shown in Figure 2. The reaction of iron with lightweight metals or metalloids in R/T fluxes to form iron clusters or layers capped by the light elements is a reoccurring theme. In addition to the two types of iron clusters reported here, carbon-capped tetrahedral Fe_4 units are found in the $\text{La}_{21}\text{Fe}_8\text{M}_7\text{C}_{12}$ structure,⁵ and aluminum-capped iron layers in $\text{La}_6\text{Fe}_{14-x}\text{Al}_x$, both grown in La/Ni flux.²² The iron cluster in $\text{R}_{33}\text{Fe}_{14-x}\text{Al}_{x+y}\text{B}_{25-y}\text{C}_{34}$ is a face capped cube (or tetrakis hexahedron) of 14 iron atoms, with six Fe2 atoms (12*e* sites) at the capping apexes and eight Fe1 sites (16*f* sites) defining the cube. The atom that centers this cluster (on the 2*a* site) is much closer to the Fe1 sites than the Fe2 sites (2.231(1) vs 2.946(1) Å in the $\text{Ce}_{33}\text{Fe}_{14-x}\text{Al}_{x+y}\text{B}_{25-y}\text{C}_{34}$ analog). The small electron density at this site indicated that it is occupied by a light atom, either B or C. The 2.231(1) Å distance from this site to the Fe1 atoms is

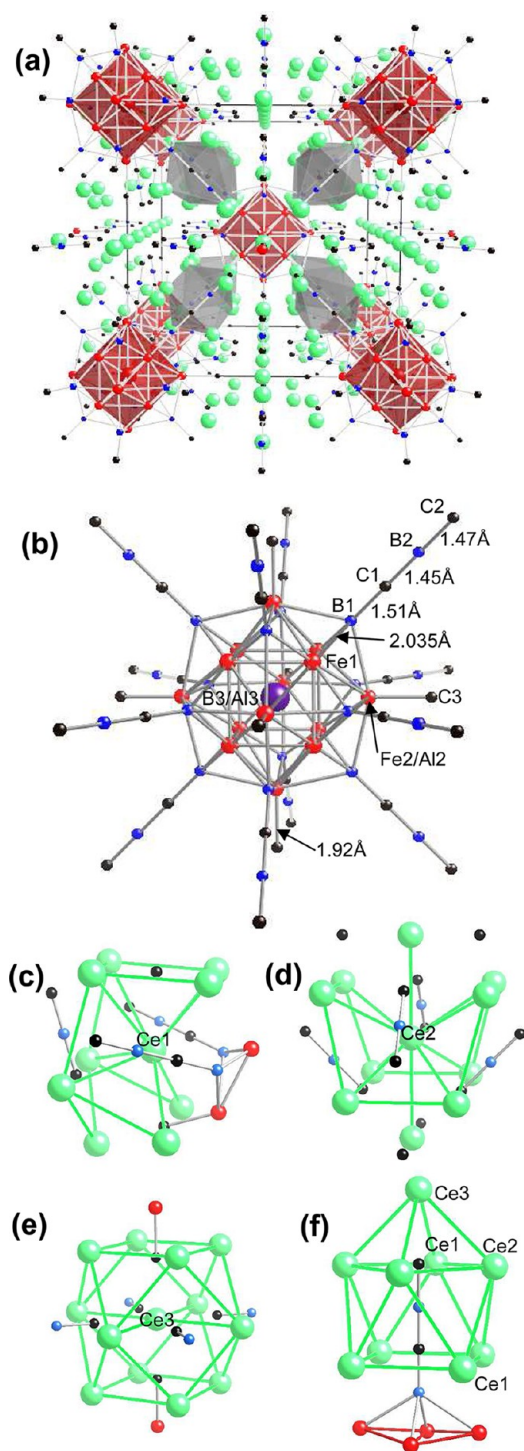


Figure 2. (a) Structure of $\text{Ce}_{33}\text{Fe}_{14}\text{Al}_1\text{B}_{24.8}\text{C}_{34}$. Red spheres are iron, green spheres are cerium, black spheres are carbon, blue spheres are boron. The boron-centered Fe_{14} clusters are drawn as red polyhedra and the isolated carbon anion in octahedral coordination as gray polyhedra. (b) Borocarbide-capped Fe_{14} cluster and associated bond lengths. (c) Ce1 coordination environment (48k site). (d) Ce2 coordination environment (12d site). (e) Ce3 coordination environment (6b site). (f) Coordination environment around the borocarbide chain.

much longer than typical Fe–C bonds in intermetallics (which are generally 2.0 Å or shorter).^{5,27} It is only slightly longer than the Fe–B bond lengths of 2.118 and 2.180 Å found in phases

such as $\text{Nd}_2\text{Fe}_{14}\text{B}$ and FeB .^{23,28} Boron is therefore a more likely option. In the $\text{Ce}_{33}\text{Mn}_{14}\text{B}_{25}\text{C}_{34}$ analog, the corresponding Mn–B bond length of 2.203(1) Å is within the range observed in MnB_4 (2.049–2.218 Å), further supporting the assignment of this site as boron.²⁹ For all analogs, allowing the occupancy to vary resulted in a higher than 100% occupancy. This, and the slightly long Fe–B bond lengths, points to incorporation of a larger, heavier element on this 2a site. It was therefore modeled as a mixture of boron and aluminum; this improved the refinement (yielding more stable thermal parameters) and indicated incorporation of 10–20% Al on this site.

The Fe_{14}B cluster in $\text{Ce}_{33}\text{Fe}_{14-x}\text{Al}_{x+y}\text{B}_{25-y}\text{C}_{34}$ features Fe–Fe bond lengths of 2.462(1) and 2.576(1) Å. These are similar to the 2.55 Å bond length in the Fe_4 clusters of $\text{La}_{21}\text{Fe}_8\text{Sn}_7\text{C}_{12}$ and well within the range of 2.429–2.740 Å observed for $\text{Ce}_2\text{Fe}_{17}$.^{5,30} In the manganese analog, the Mn–Mn bond lengths (2.462(1) and 2.544(1) Å) in the Mn_{14}B cluster compare well with those found in $\beta\text{-Mn}$ which range from 2.363 to 2.680 Å.³¹ A small amount of Al substitution (15%) is observed for the Fe2 sites of $\text{Ce}_{33}\text{Fe}_{14-x}\text{Al}_{x+y}\text{B}_{25-y}\text{C}_{34}$. No Al substitution on the Mn sites was observed based on the refinement of the occupancies of these atoms from the single crystal data of $\text{Ce}_{33}\text{Mn}_{14}\text{B}_{25}\text{C}_{34}$, but trace amounts of Co observed in the EDXS analysis suggest there may be incorporation of cobalt from the flux on these sites.

The iron clusters are capped at the six vertices by carbon atoms, and capped on 12 edges by 4-atom linear chains of carbon and boron (Figure 2b). The title compounds thus add to the small database of reported structures containing borocarbide chains, which includes $\text{R}_{10}\text{B}_9\text{C}_{12}$ (R = La, Ce, Pr, Nd), $\text{R}_5\text{B}_2\text{C}_5$ (R = Ce–Tm), $\text{R}_5\text{B}_4\text{C}_5$ (R = Ce, Pr, Nd), RBC (R = Ce, Pr, Nd), $\text{R}_{15}\text{B}_6\text{C}_{20}$, CeB_2C_2 , Lu_3BC_3 , and $\text{Gd}_4\text{B}_3\text{C}_4$.^{32–39} Assignments of the carbon and boron sites in these chains were made based on bond lengths within the chain and distances to cerium atoms surrounding this chain, and comparison to other metal borocarbide structures. The B1 site caps an edge of the Fe_{14}B cluster; it is bonded to 2 Fe atoms, 1 C atom, and 4 Ce atoms. The associated bond lengths are shown in Figure 2b and listed in Table 3. These bond lengths compare well with those reported for similar compounds such as CeB_2C_2 , with a Ce–B bond distance of 2.8402(2) Å and B–C bond distances of 1.5312(9)–1.6220(6) Å.³⁷ The rest of the $\text{Ce}_{33}\text{Fe}_{14-x}\text{Al}_{x+y}\text{B}_{25-y}\text{C}_{34}$ borocarbide chain extends from the B1 atom, with bond distances between the C1–B2–C2 atoms of C1–B2 of 1.45(1) Å and B2–C2 of 1.47(1) Å. These are similar to the 1.44–1.48 Å range of bond lengths observed in other compounds containing linear C–B–C units such as $\text{Gd}_4\text{B}_3\text{C}_4$ and Lu_3BC_3 .^{38,39} Termination of these chains by C atoms is thought to be favored due to the surrounding octahedral coordination environment, and on the basis of the higher electronegativity of carbon and its affinity for the electropositive rare earth ions.⁴⁰ The distances from atoms in the borocarbide chain of $\text{Ce}_{33}\text{Fe}_{14-x}\text{Al}_{x+y}\text{B}_{25-y}\text{C}_{34}$ to the surrounding cerium ions exhibit the expected trend of shorter Ce–C bonds (all below 2.8005(6) Å) and longer Ce–B bonds (all above 2.871(3) Å); see Figure 2f.

The $\text{R}_{33}\text{Fe}_{14-x}\text{Al}_{x+y}\text{B}_{25-y}\text{C}_{34}$ structure also features an isolated carbon site (C4) surrounded by six cerium cations in an octahedral configuration. These carbide anions (presumably C^{4-}) and their coordination environment are depicted as gray octahedra in Figure 2. The six R–C bond lengths are all equal and are only slightly affected by replacing Fe with Mn in the

Table 3. Bond Lengths (in Å) for Selected R/T/B/C Phases

	$\text{Ce}_{33}\text{Fe}_{13,1}\text{Al}_{1,1}\text{B}_{24,8}\text{C}_{34}$		$\text{Ce}_{33}\text{Fe}_{13}\text{B}_{18}\text{C}_{34}$	$\text{Pr}_{33}\text{Fe}_{12,9}\text{Al}_{0,1}\text{B}_{18}\text{C}_{34}$
Ce1–C4	2.6576(4)	R1–C4	2.630(1)	2.6471(3)
Ce1–C1	2.672(1)	R1–C1	2.580(1)	2.5912(5)
Ce1–B1	2.871(3)	R1–B1	3.053(5)	3.058(4)
Ce1–Ce1	3.7274(6)	R1–R1	3.601(2)	3.6356(4)
Ce1–Ce2	3.8089(4)			
Ce2–Ce3	3.6543(3)	R2–R3	3.562(1)	3.5970(2)
B1–C1	1.507(11)	B1–C1	1.501(11)	1.469(10)
B1–Fe1	2.035(6)	C2–B1	1.499(11)	1.500(10)
B1–Fe2	2.462(4)	C3–B2	1.579(19)	1.667(21)
C1–B2	1.445(11)	R1–B2	2.854(6)	2.913(6)
B2–Ce2	2.941(4)			
B2–Ce1	3.100(4)	R1–C3	2.563(2)	2.588(2)
C2–B2	1.469(11)	R1–Fe1	3.148(2)	3.1581(6)
C2–Ce3	2.519(8)	R2–C2	2.519(1)	2.5450(3)
C2–Ce2	2.5848(3)	R2–B1	2.946(5)	2.998(4)
C2–Ce1	2.8007(5)			
Fe1–B3	2.231(1)	Fe1–B2	2.236(8)	2.200(8)
Fe1–Fe2	2.462(1)	Fe1–Fe1	2.579(2)	2.598(1)
Fe1–Fe1	2.576(1)	Fe1–Fe2	2.579(2)	2.598(1)
Fe2–C3	1.917(17)	Fe1–C1	1.947(8)	1.976(7)
C3–Ce3	2.447(17)			

structure (Ce–C distances 2.6576(4) and 2.657(2) Å for the Fe and Mn analogs, respectively).

Structure of $\text{R}_{33}\text{Fe}_{13-x}\text{Al}_x\text{B}_{18}\text{C}_{34}$ (R = Ce, Pr). $\text{R}_{33}\text{Fe}_{13-x}\text{Al}_x\text{B}_{18}\text{C}_{34}$ crystallizes in the centrosymmetric space group $Im\bar{3}m$, with unit cell parameters of $a = 14.246(8)$ Å for the Ce analog and $a = 14.3881(9)$ Å for the Pr analog. The Fe_{13} iron cluster in this structure is perfectly cuboctahedral and is centered by another iron atom instead of a boron atom (see Figure 3). The Fe–Fe bond lengths between neighboring iron atoms and those to the center iron are all equal; this distance of 2.579(2) Å for the cerium analog is slightly longer than the distances seen for $\text{Ce}_{33}\text{Fe}_{14-x}\text{Al}_{x+y}\text{B}_{25-y}\text{C}_{34}$ and $\text{La}_{21}\text{Fe}_8\text{Sn}_7\text{C}_{12}$, but is well within the ranges seen in $\text{Ce}_2\text{Fe}_{17}$ and $\alpha\text{-Fe}$ (2.482–2.866 Å).^{5,30} A very small amount of aluminum substitution (4%) is seen on the central Fe2 site for $\text{Pr}_{33}\text{Fe}_{12,9}\text{Al}_{0,1}\text{B}_{18}\text{C}_{34}$, but not for the cerium analogue. All 12 of the Fe1 atoms defining the cuboctahedron are capped by a C–B–C chain. The Fe1–C1 bond is 1.947(8) Å in length; subsequent bond lengths in the chain are C1–B1 of 1.50(1) Å and B1–C2 of 1.50(1) Å, comparing well to those in other structures. The six square faces of the cuboctahedron are each capped by a B–C unit with a Fe1–B2 distance of 2.236(8) Å, very similar to the distances between the Fe_{14}B cluster to the capping BCBC chains in $\text{Ce}_{33}\text{Fe}_{14-x}\text{Al}_{x+y}\text{B}_{25-y}\text{C}_{34}$. The B2–C3 distance of 1.58(2) Å is somewhat longer than expected, but the distances from the C3 site to surrounding rare earth ions support the assignment of this site as carbon and not boron. All terminal C atoms are bonded to Ce atoms at distances of 2.43(1)–2.717(1) Å, forming a framework that surrounds the central Fe cluster. As is seen in the $\text{R}_{33}\text{Fe}_{14-x}\text{Al}_{x+y}\text{B}_{25-y}\text{C}_{34}$ structure, $\text{R}_{33}\text{Fe}_{13-x}\text{Al}_x\text{B}_{18}\text{C}_{34}$ also features isolated C^{4-} anions (C4 sites) octahedrally coordinated by R cations with six equivalent C–Ce distances of 2.630(1) Å.

It is notable that $\text{Ce}_{33}\text{Fe}_{13}\text{B}_{18}\text{C}_{34}$ has a smaller unit cell than its praseodymium analog. All bond lengths associated with rare earth sites are shorter in the Ce phase compared to the Pr analog (see Table 3), contrary to what is expected given the relative sizes of Ce^{3+} and Pr^{3+} . The Ce–X bonds are also

shorter than similar bonds in $\text{Ce}_{33}\text{Fe}_{14-x}\text{Al}_{x+y}\text{B}_{25-y}\text{C}_{34}$, with Ce–Ce bonds in particular shrinking from 3.6543(3) and 3.7274(6) Å in the latter to 3.562(1) and 3.601(2) Å in $\text{Ce}_{33}\text{Fe}_{13}\text{B}_{18}\text{C}_{34}$. This indicates a high likelihood of the presence of Ce^{4+} in $\text{Ce}_{33}\text{Fe}_{13}\text{B}_{18}\text{C}_{34}$. To confirm this, XPS data were collected on crystals of $\text{Ce}_{33}\text{Fe}_{13}\text{B}_{18}\text{C}_{34}$. After sputtering to remove surface oxide species, the spectrum features two broad peaks at binding energies of 900 and 918 eV (see Figure S2 in Supporting Information), with associated shake-down peaks at 895 and 913 eV. These correspond to a $3d_{5/2}$ – $3d_{3/2}$ spin–orbit doublet which arises exclusively from Ce^{4+} ; the 918 eV peak in particular does not overlap with any possible transitions characteristic of Ce^{3+} and is viewed as strongly indicative of tetravalent cerium.^{41,42}

The formation of tetravalent cerium in this compound may be induced by chemical pressure. The $\text{R}_{33}\text{Fe}_{13}\text{B}_{18}\text{C}_{34}$ structure is stable for the smaller rare earth cation Pr^{3+} ; the packing of the Fe_{13} clusters and associated borocarbide chains promotes the conversion of Ce^{3+} cations to smaller Ce^{4+} ions to stabilize the compound. Similar effects are seen for systems such as $\text{Ce}_x\text{Y}_{1-x}\text{Al}_3$, where substitution of smaller Y^{3+} into the rare earth sites causes the average surrounding coordination environment to shrink and induces formation of Ce^{4+} ions.⁴³

Transport Properties of $\text{Ce}_{33}\text{Fe}_{14-x}\text{Al}_{x+y}\text{B}_{25-y}\text{C}_{34}$. Resistivity measurements performed on a single crystal of $\text{Ce}_{33}\text{Fe}_{14-x}\text{Al}_{x+y}\text{B}_{25-y}\text{C}_{34}$ indicate that this material behaves as a poor metal (see Figure 4). The room temperature resistivity is 5.39 Ω cm; this lies in the overlap of typical metallic (10^{-5} – 10^1 Ω cm) and semiconductor (10^{-2} – 10^5 Ω cm) resistivity ranges.⁴⁴ The resistivity rises as the temperature is increased, as is expected for metals. Two kinks in the temperature dependence are observed, one at low temperature (10 K) which corresponds to a magnetic ordering transition, and one at 125 K which may be due to cerium fluctuating valence; both these features are mirrored in the magnetic susceptibility data (vide infra).

NMR studies were carried out on $\text{Ce}_{33}\text{Fe}_{14-x}\text{Al}_{x+y}\text{B}_{25-y}\text{C}_{34}$ in an attempt to glean information about boron and carbon siting

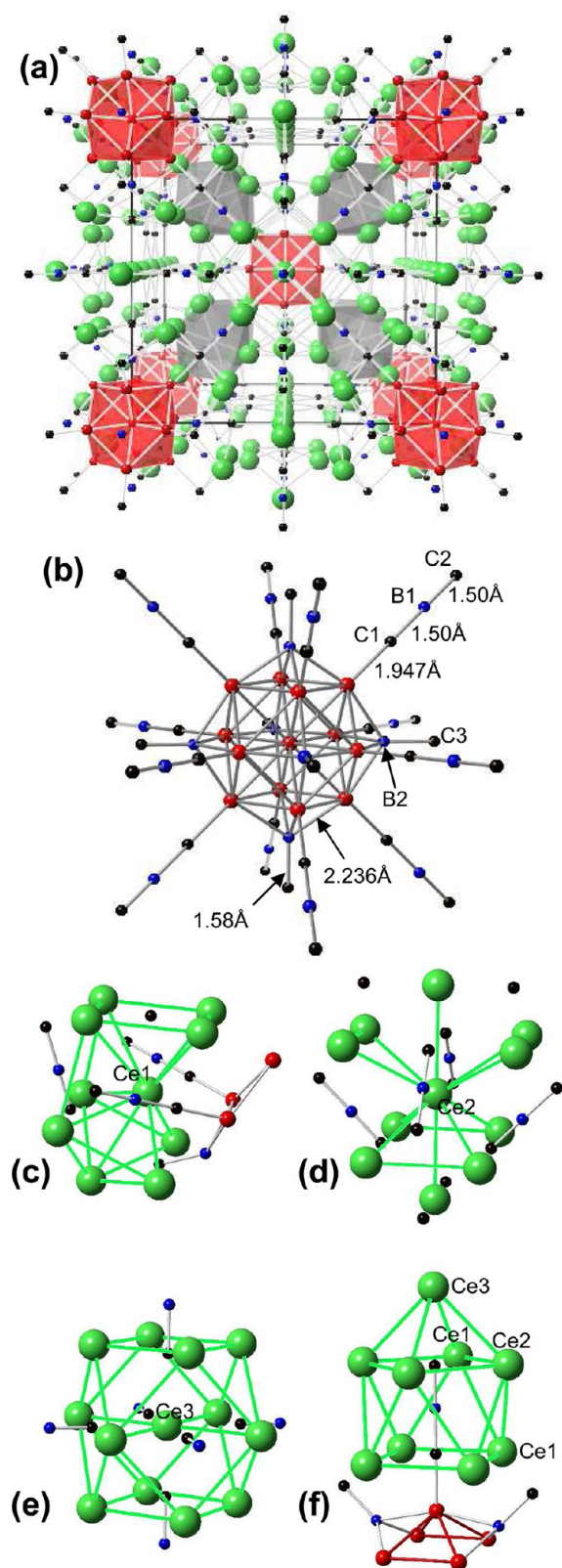


Figure 3. (a) Structure of $\text{Ce}_{33}\text{Fe}_{13}\text{B}_{18}\text{C}_{34}$. Red spheres are iron, green spheres are cerium, black spheres are carbon, blue spheres are boron. The cuboctahedral Fe_{13} clusters are drawn as red polyhedra and the isolated carbon anion in octahedral coordination as gray polyhedra. (b) Fe_{13} cluster and associated bond lengths. (c) Ce1 coordination environment (48k site). (d) Ce2 coordination environment (12d site). (e) Ce3 coordination environment (6b site). (f) Coordination environment around the borocarbide chain.

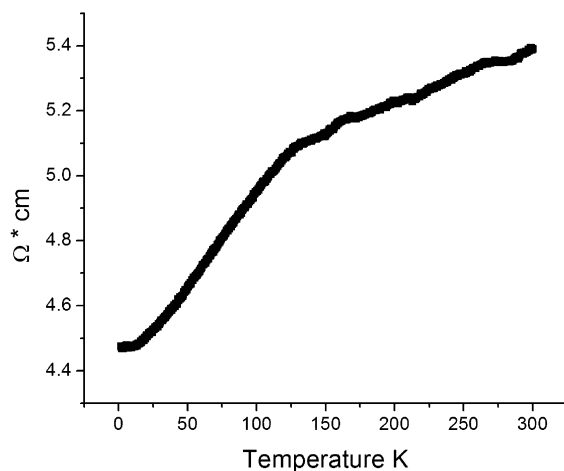


Figure 4. Resistivity data for $\text{Ce}_{33}\text{Fe}_{14-x}\text{Al}_{x+y}\text{B}_{25-y}\text{C}_{34}$, measured on a single crystal.

as well as the interaction of these nuclei with conduction electrons. While no ^{13}C resonances could be observed (likely due to low natural abundance and broadening from surrounding paramagnetic atoms), the ^{11}B MAS NMR spectrum shows a single peak at 11.2 ppm (Figure S3, Supporting Information). This is likely due to the B2 site, which is bonded to two carbon atoms; the resonances of the two other boron sites (both bonded directly to iron) may be too broadened to be observed. This ^{11}B shift is similar to those reported for YB_4 , LaB_4 and $\text{CaC}_x\text{B}_{4-x-y}$, all of which have resonances in the 5–56 ppm range.^{45,46} In these phases, the small shift (relative to the larger Knight shifts expected for metals) is attributed to a small boron s-electron density of states at the Fermi level. Polar intermetallic phases often feature a pseudogap in the DOS at E_F ⁴⁷ which can lead to poor conductivity and a small Knight shift. The NMR data and resistivity measurements suggest that $\text{Ce}_{33}\text{Fe}_{14-x}\text{Al}_{x+y}\text{B}_{25-y}\text{C}_{34}$ may exhibit such a pseudogap, leading to poor metal behavior.

Magnetic Behavior of $\text{R}_{33}\text{Fe}_{14-x}\text{Al}_{x+y}\text{B}_{25-y}\text{C}_{34}$ Phases. The magnetic properties of $\text{R}_{33}\text{Fe}_{14-x}\text{Al}_{x+y}\text{B}_{25-y}\text{C}_{34}$ and $\text{R}_{33}\text{Fe}_{13-x}\text{Al}_x\text{B}_{18}\text{C}_{34}$ phases are of particular interest, given the presence of two potentially paramagnetic species: the iron clusters and the rare earth cations. The magnetic susceptibility of $\text{La}_{33}\text{Fe}_{14-x}\text{Al}_{x+y}\text{B}_{25-y}\text{C}_{34}$ is small and roughly temperature independent (see Figure 5), indicating Pauli paramagnetic behavior and therefore no magnetic moment on the iron atoms. The slight Curie tail at low temperature is likely due to traces of oxidation or paramagnetic impurities on the surface of the crystal sample. The magnitude of the Pauli paramagnetism (0.06 emu/mol; taking the stoichiometry into account, this corresponds to roughly 1×10^{-3} emu/mol of metal atoms) is consistent with that seen for other metallic compounds.⁴⁸ The cerium analog $\text{Ce}_{33}\text{Fe}_{14-x}\text{Al}_{x+y}\text{B}_{25-y}\text{C}_{34}$ was studied using susceptibility measurements, XPS measurements to investigate cerium valence, and Mössbauer studies on an 57-Fe enriched sample to explore possible magnetic transitions of iron sites. The temperature dependence of the susceptibility (Figure 5) shows paramagnetic behavior above 200 K which can be fit to a modified Curie–Weiss law ($\chi = (C/T - \theta) + \chi_p$, where C is the Curie constant, θ is the Weiss temperature, and χ_p corresponds to the Pauli paramagnetism of the conduction electrons). The resulting parameters, listed in Table 4, indicate an effective magnetic moment per cerium ion of $2.36 \mu_B$, which is only

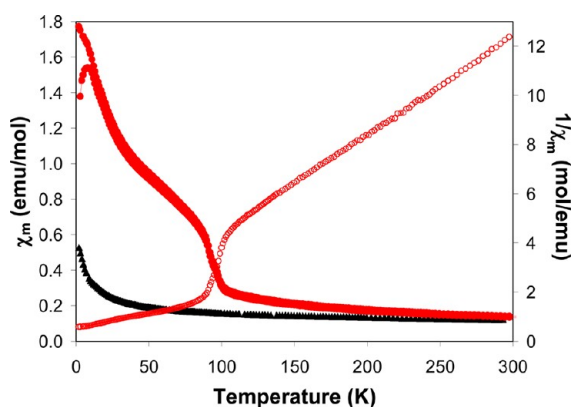


Figure 5. Temperature dependence of magnetic susceptibility for $R_{33}Fe_{14-x}Al_{x+y}B_{25-y}C_{34}$ phases, with an applied field of 100 Oe. Data for La analog are in black; data for Ce analog (filled circles χ_m and open circles $1/\chi_m$) are in red.

Table 4. Magnetic Data for R/Fe/B/C Phases

compound	moment per R^{3+} ion (μ_B)	θ (K)	χ_P (emu/mol of FU)	observed transition
$La_{33}Fe_{14}B_{25}C_{34}$			0.06	Pauli paramagnetic
$Ce_{33}Fe_{14}B_{25}C_{34}$	2.36	-8.4	0.06	AF; $T_N = 9$ K
$Ce_{33}Fe_{13}B_{18}C_{34}$		non-Curie-Weiss		FM; $T_C = 190$ K
$Pr_{33}Fe_{13}B_{18}C_{34}$	4.15	-44	0.06	AF; $T_N = 16$ K

slightly lower than the theoretical value of $2.54 \mu_B$ for Ce^{3+} ions.⁴⁸ The negative Weiss constant of $\theta = -8.4$ K indicates the presence of antiferromagnetic coupling forces, in agreement with the observed antiferromagnetic ordering at $T_N = 9$ K. This ordering is likely due to the cerium ions; as in the La analog, the iron atoms in $Ce_{33}Fe_{14-x}Al_{x+y}B_{25-y}C_{34}$ do not appear to have a magnetic moment.

The lack of magnetic moment on the iron atoms in $R_{33}Fe_{14-x}Al_{x+y}B_{25-y}C_{34}$ phases is somewhat surprising considering the magnetic behavior exhibited by iron atoms in the smaller Fe_4 clusters of $La_{21}Fe_8Sn_7C_{12}$.⁵ The quenching of the iron magnetism may be due to the $Fe_{14}B$ clusters of $R_{33}Fe_{14-x}Al_{x+y}B_{25-y}C_{34}$ being "diluted" by the central boron atom and by the aluminum substitution on the Fe(2) site. Similar dilution effects are observed for $R_2Fe_{14}B$ phases and their substituted analogs. In the $Nd_2Fe_{14}B$ structure, the iron sites with the largest number of iron nearest neighbors have the largest magnetic moments, and the moments of all the iron atoms are lowered when $R_2Fe_{14-x}T_xB$ analogs are made with iron diluted by a nonmagnetic element T.¹⁶ The $La(Al_xFe_{1-x})_{13}$ family of compounds exhibits a similar drop in the iron magnetic moment as the amount of Al substitution increases.⁴⁹

The other notable feature in the susceptibility data of $Ce_{33}Fe_{14-x}Al_{x+y}B_{25-y}C_{34}$ is a broad bump from 75 to 150 K. This is reproducibly seen in the magnetic data for several different samples of this compound. It also corresponds to the kink in the resistivity temperature dependence shown in Figure 4. Mössbauer spectra were collected at several temperatures spanning this transition to determine if it is caused by the iron sites. The data taken at 78, 150, and 294 K are shown in Figure 6; the spectra consist of a broad peak with a shoulder (in agreement with the presence of two iron sites in the structure). No hyperfine splitting or variation in shift is observed between 78 and 294 K. Also, field dependence magnetization data taken at various temperatures in this range (Figure 7) show normal

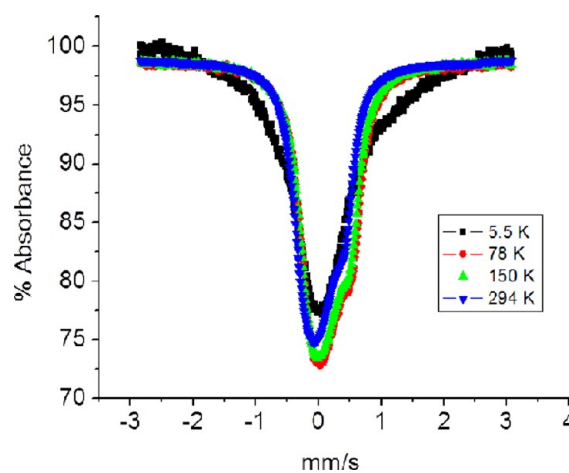


Figure 6. ^{57}Fe Mössbauer spectra at various temperatures for ^{57}Fe enriched sample of $Ce_{33}Fe_{14-x}Al_{x+y}B_{25-y}C_{34}$.

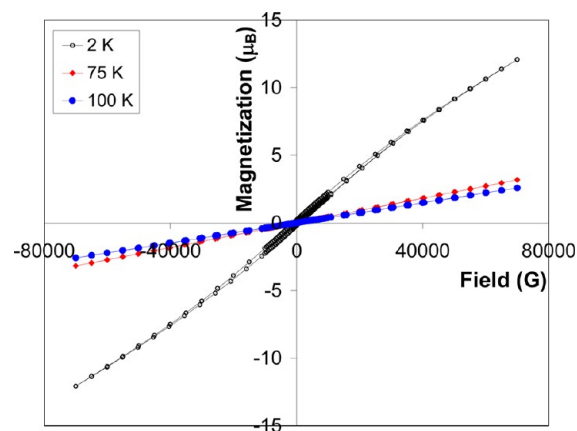


Figure 7. Magnetization data for $Ce_{33}Fe_{14-x}Al_{x+y}B_{25-y}C_{34}$ at several temperatures.

linear paramagnetic behavior. Therefore, this transition at around 120 K does not appear to be a magnetic ordering phenomenon and is not associated with the iron sites. The fact that this feature is not seen in the data for the lanthanum analog indicates that it may be due to fluctuating valence of the cerium ions. The Curie-Weiss fit of the susceptibility temperature dependence supports the presence of Ce^{3+} at high temperature. This is also supported by room temperature XPS data on $Ce_{33}Fe_{14-x}Al_{x+y}B_{25-y}C_{34}$ (Figure S4, Supporting Information) which show the $Ce 3d_{5/2}$ and $3d_{3/2}$ peaks and their satellites in positions typical for Ce^{3+} ; the spectrum is very similar to those seen for $CePO_4$ and $CeFeAsO$.^{42,50} However, as the temperature is lowered below 150 K, thermal contraction of the lattice may become sufficient to promote Ce^{3+}/Ce^{4+} valence fluctuation. One or more of the three cerium sites may remain trivalent; these remaining paramagnetic ions order antiferromagnetically at 9 K. Similar behavior is seen in the mixed valent phase $Ce_{23}Ru_7Cd_4$, where 20 out of the 46 cerium ions in the cell remain trivalent and their magnetic moments order at 3.6 K.¹⁰ The ^{57}Fe Mössbauer spectra of $Ce_{33}Fe_{14-x}Al_{x+y}B_{25-y}C_{34}$ (Figure 6) show very little change below the antiferromagnetic transition at 9 K; instead of hyperfine splitting, only a slight broadening is observed in the 5.5 K spectrum which indicates weak coupling of the iron with the surrounding Ce^{3+} ions as they undergo their ordering transition.

Magnetic Behavior of $R_{33}Fe_{13-x}Al_xB_{18}C_{34}$ Phases. The magnetic susceptibility data for $Ce_{33}Fe_{13}B_{18}C_{34}$ are shown in Figure 8. The dominant feature is a distinct rise in susceptibility

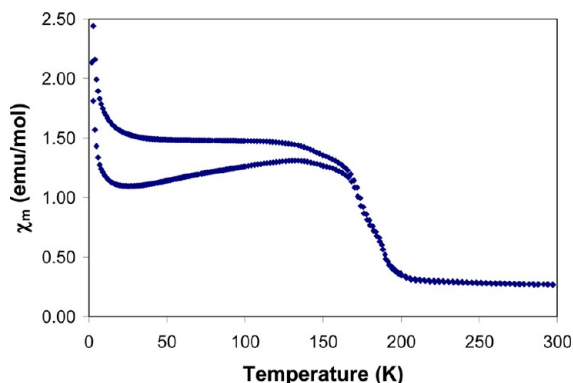


Figure 8. Temperature dependence of magnetic susceptibility for $Ce_{33}Fe_{13}B_{18}C_{34}$ at 100 Oe applied field.

at 180 K and subsequent field-cooled/zero-field-cooled splitting at lower temperatures. Since the room temperature XPS data (Figure S2, Supporting Information) indicate that this phase contains diamagnetic Ce^{4+} ions, this rise in susceptibility is likely due to magnetic ordering of the iron clusters. Field dependence data (Figure 9) taken above and below the

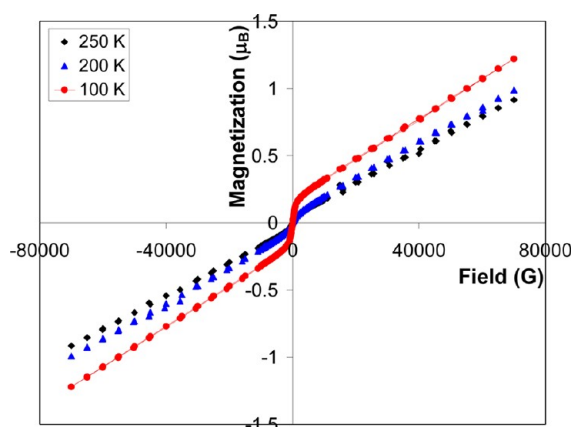


Figure 9. Field dependence of magnetization for $Ce_{33}Fe_{13}B_{18}C_{34}$ at several different temperatures.

transition at 150 K show an increase in magnetization below this temperature, confirming that the rise in susceptibility is magnetic in origin. The nature of the magnetic ordering is not clear; the magnetization is not saturated, which may indicate that the magnetic coupling and ferri- or ferromagnetic ordering occurs within individual Fe_{13} clusters, but not between them (each cluster is 12.3 Å away from eight neighboring clusters). The data above the ordering temperature cannot be fit to the Curie–Weiss law, so determination of the iron moment is not possible. The fact that the iron atoms in this structure have magnetic moments while the Fe_{14} clusters in $Ce_{33}Fe_{14-x}Al_{x+y}B_{25-y}C_{34}$ do not is likely due to the fact that the Fe_{13} clusters are not diluted by a central boron atom or small amounts of Al substitution on the iron sites.

The magnetic susceptibility data for the $Pr_{33}Fe_{13-x}Al_xB_{18}C_{34}$ analog, shown in Figure 10, can be fit to the Curie–Weiss law above 100 K. This yields a magnetic moment of $4.15 \mu_B$ per

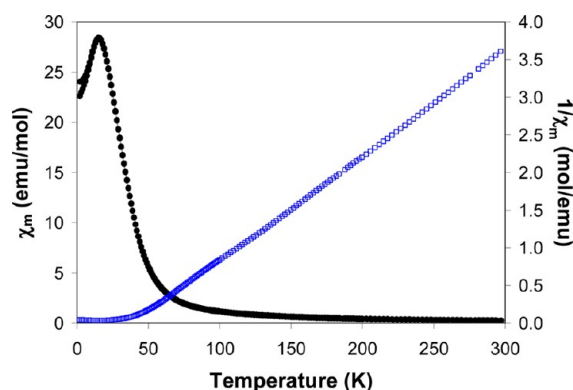


Figure 10. Temperature dependence of magnetic susceptibility for $Pr_{33}Fe_{13-x}Al_xB_{18}C_{34}$ with an applied field of 100 Oe. Filled black circles χ_m and open blue circles $1/\chi_m$.

praseodymium ion, significantly higher than the $3.58 \mu_B$ expected for Pr^{3+} .⁴⁸ The higher moment indicates that the iron atoms in this phase exhibit magnetic moments, as is seen for $Ce_{33}Fe_{13}B_{18}C_{34}$. However, no ferromagnetic ordering is observed that would correspond to the transition at 180 K seen for the cerium compound. This lack of ordering may be due to the small amount of aluminum substitution consistently observed in the EDS and crystallographic data for this analog. This, and the slightly longer Fe–Fe bonds in the iron clusters (2.598 Å in $Pr_{33}Fe_{13-x}Al_xB_{18}C_{34}$ vs 2.579 Å in the cerium analog), may hinder ordering of the magnetic moments. The low temperature antiferromagnetic ordering observed at 16 K is likely due to the moments on the Pr^{3+} ions; antiferromagnetic coupling is supported by the negative Weiss constant of -44 K.

CONCLUSION

The two Ce/Fe/B/C intermetallic compounds grown in Ce/T flux have similar structures, but the cerium and iron atoms in these phases exhibit very different behaviors. The Fe_{14} clusters in $Ce_{33}Fe_{14-x}Al_{x+y}B_{25-y}C_{34}$ are nonmagnetic due to dilution of Fe–Fe bonding by boron and aluminum; the iron atoms in the Fe_{13} clusters in $Ce_{33}Fe_{13}B_{18}C_{34}$ do exhibit magnetic moments and ordering. These two borocarbide-capped iron clusters offer a “missing link” between isolated iron sites in intermetallics and more extended iron building blocks such as iron layers and networks featuring extensive Fe–Fe bonding. $Ce_{33}Fe_{13}B_{18}C_{34}$ is an ordered array of identical magnetic iron nanoclusters; it is not clear if these relatively isolated Fe_{13} clusters are interacting. Further studies on the magnetism of this phase are planned, although the synthesis yield must be improved for ^{57}Fe enrichment (for Mössbauer studies) or ^{11}B enrichment to allow neutron diffraction studies.

Both Ce/Fe/B/C structures feature three crystallographically unique cerium sites. All of the cerium ions in $Ce_{33}Fe_{14-x}Al_{x+y}B_{25-y}C_{34}$ are trivalent at high temperature, but some convert to Ce^{4+} below 100 K. $Ce_{33}Fe_{13}B_{18}C_{34}$ appears to feature predominantly tetravalent cerium ions. Both these behaviors can be explained by the presence of different forms of chemical pressure. The normal thermal contraction of bonds occurring as $Ce_{33}Fe_{14-x}Al_{x+y}B_{25-y}C_{34}$ cools is evidently sufficient to trigger conversion of some cerium sites from Ce^{3+} to Ce^{4+} . The squeezing of cerium ions into the $R_{33}Fe_{13}B_{18}C_{34}$ structure (which is more stable for smaller Pr^{3+} cations) stabilizes the tetravalent state. Experiments to

substitute smaller R³⁺ cations into these structures to observe the effects are underway.

■ ASSOCIATED CONTENT

■ Supporting Information

Table of atomic positions and displacement factors for R/Fe/B/C compounds. Powder diffraction data, XPS data for cerium phases, ¹¹B MAS NMR spectrum for Ce₃₃Fe_{14-x}Al_{x+y}B_{25-y}C₃₄. Additional crystallographic data for all phases (CIF). This material is available free of charge via the Internet at <http://pubs.acs.org>.

■ AUTHOR INFORMATION

Corresponding Author

lattur@chem.fsu.edu

Notes

The authors declare no competing financial interest.

■ ACKNOWLEDGMENTS

This work made use of the NMR facilities of the Department of Chemistry and Biochemistry, the SEM facilities of the Department of Physics, and facilities at the National High Magnetic Field Laboratory. Financial Support from the NSF (grants DMR-05-47791 and DMR-11-06150) is gratefully acknowledged. We thank Dr. Eric Lochner for his assistance in obtaining the XPS data. Mössbauer spectra were taken at the NHMFL which is funded by the NSF through Cooperative Agreement No. DMR-06-54118, the State of Florida, and the DOE. The Mössbauer instrument was purchased using the User Collaboration Grant Program 5064 funds awarded to A.O.

■ REFERENCES

- (1) Kanatzidis, M. G.; Pöttgen, R.; Jeitschko, W. *Angew. Chem., Int. Ed.* **2005**, *44*, 6996–7023.
- (2) Stojanovic, M.; Lattur, S. E. *J. Solid State Chem.* **2007**, *180*, 907–914.
- (3) Reynolds, P. C.; Stojanovic, M.; Lattur, S. E. *J. Solid State Chem.* **2011**, *184*, 1875–1881.
- (4) Lang, D. A.; Zaikina, J. V.; Lovingood, D. D.; Gedris, T. E.; Lattur, S. E. *J. Am. Chem. Soc.* **2010**, *132*, 17523–17530.
- (5) (a) Benbow, E. M.; Dalal, N.; Lattur, S. E. *J. Am. Chem. Soc.* **2009**, *131*, 3349–3354. (b) Zaikina, J. V.; Schellenberg, I.; Benbow, E. M.; Pöttgen, R.; Lattur, S. E. *Chem. Mater.* **2011**, *23*, 1768–1778.
- (6) Zaikina, J. V.; Jo, Y. J.; Lattur, S. E. *Inorg. Chem.* **2010**, *49*, 2773–2781.
- (7) Zaikina, J. V.; Zhou, H.; Lattur, S. E. *J. Solid State Chem.* **2010**, *183*, 2987–2994.
- (8) Kirchmayr, H. R.; Poldy, C. A. *J. Magn. Magn. Mater.* **1978**, *8*, 1–42.
- (9) Reehuis, M.; Brown, P. J.; Jeitschko, W.; Moller, M. H.; Vomhof, T. *J. Phys. Chem. Solids* **1993**, *54*, 469–475.
- (10) Tappe, F.; Hermes, W.; Eul, M.; Pöttgen, R. *Intermetallics* **2009**, *17*, 1035–1040.
- (11) Mishra, R.; Hermes, W.; Rodewald, U. C.; Hoffmann, R. D.; Pöttgen, R. *Z. Anorg. Allg. Chem.* **2008**, *634*, 470–474.
- (12) Hegger, H.; Petrovic, C.; Moshopoulou, E. G.; Hundley, M. F.; Sarrao, J. L.; Fisk, Z.; Thompson, J. D. *Phys. Rev. Lett.* **2000**, *84*, 4986–4989.
- (13) Witte, A. M.; Jeitschko, W. *Z. Naturforsch. B* **1996**, *51*, 249–256.
- (14) Sieve, B.; Gray, D. L.; Henning, R.; Bakas, T.; Schultz, A. J.; Kanatzidis, M. G. *Chem. Mater.* **2008**, *20*, 6107–6115.
- (15) McCallum, R. W.; Fisher, I. R.; Anderson, N. E.; Canfield, P. C.; Kramer, M. J.; Dennis, K. W. *IEEE Trans. Magn.* **2001**, *37*, 2147–2149.
- (16) Szytula, A.; Leciejewicz, J. *CRC Handbook of Crystal Structures and Magnetic Properties of Rare Earth Intermetallics*; CRC Press: Boca Raton, FL, 1994.
- (17) Massalski, T. B.; Okamoto, H. *Binary Alloy Phase Diagrams*, 2nd ed.; ASM International: Materials Park, OH, 1990.
- (18) *SAINT*, version 6.02a; Bruker AXS Inc.: Madison, WI, 2000.
- (19) Sheldrick, G. M. *SHELXTL NT/2000*, version 6.1; Bruker AXS, Inc.: Madison, WI, 2000.
- (20) Dashjav, E.; Kreiner, G.; Schnelle, W.; Wagner, F. R.; Kniep, R.; Jeitschko, W. *J. Solid State Chem.* **2007**, *180*, 636–653.
- (21) Davaasuren, B.; Borrmann, H.; Dashjav, E.; Kreiner, G.; Widom, M.; Schnelle, W.; Wagner, F. R.; Kniep, R. *Angew. Chem., Int. Ed.* **2010**, *49*, 5688–5692.
- (22) Benbow, E. M.; Dalal, N. S.; Lattur, S. E. *J. Solid State Chem.* **2009**, *182*, 3055–3062.
- (23) Villars, P.; Calvert, L. D. *Pearson's Handbook—Crystallographic Data for Intermetallic Phases*; ASM International: Materials Park, OH, 1998.
- (24) Peter, S. C.; Malliakos, C. D.; Nakotte, H.; Kothapilli, K.; Rayaprol, S.; Schultz, A. J.; Kanatzidis, M. G. *J. Solid State Chem.* **2012**, *187*, 200–207.
- (25) Salvador, J. R.; Birc, D.; Mahanti, S. D.; Kanatzidis, M. G. *Angew. Chem., Int. Ed.* **2003**, *42*, 1929–1932.
- (26) Wagner, C. D.; Naumkin, A. V.; Kraut-Vass, A.; Allison, J. W.; Powell, C. J.; Rumble, J. R. *NIST X-ray Photoelectron Spectroscopy Database*, Version 3.5; National Institute of Standards and Technology: Gaithersburg, 2003; <http://srdata.nist.gov/xps/>.
- (27) Gerss, M. H.; Jeitschko, W.; Boonk, L.; Nientiedt, J.; Grobe, J.; Morsen, E.; Leson, A. *J. Solid State Chem.* **1987**, *70*, 19–28.
- (28) Shoemaker, C. B.; Shoemaker, D. P.; Fruchart, R. *Acta Cryst. C* **1984**, *40*, 1665–1668.
- (29) Anderson, S.; Carlsson, J. O. *Acta Chem. Scand.* **1970**, *24*, 1791–1799.
- (30) Tepykh, P. A.; Pirogov, A. N.; Kuchin, A. G.; Tepykh, A. E. *Phys. B* **2004**, *350*, E99–E102.
- (31) Shoemaker, C. B.; Shoemaker, D. P.; Hopkins, T. E.; Yindepit, S. *Acta Cryst. B* **1978**, *34*, 3573–3576.
- (32) Babizhetskyy, V.; Hiebl, K.; Kremer, R. K.; Mattausch, H.; Simon, A. *Solid State Sci.* **2007**, *9*, 1126–1134.
- (33) Bidaud, E.; Hiebl, K.; Hoffmann, R. D.; Pöttgen, R.; Jardin, C.; Bauer, J.; Gautier, R.; Gougeon, P.; Saillard, J. Y.; Halet, J. F. *J. Solid State Chem.* **2000**, *154*, 286–295.
- (34) Babizhetskyy, V.; Hiebl, K.; Mattausch, H.; Simon, A. *J. Phys. Chem. Solids* **2009**, *70*, 561–566.
- (35) Babizhetskyy, V.; Hiebl, K.; Mattausch, H.; Simon, A. *Solid State Sci.* **2009**, *11*, 501–506.
- (36) Babizhetskyy, V.; Mattausch, H.; Simon, A.; Hiebl, K.; Yahia, M. B.; Gautier, R.; Halet, J. F. *J. Solid State Chem.* **2008**, *181*, 1882–1890.
- (37) vanDuijn, J.; Suzuki, K.; Atfield, J. P. *Angew. Chem.* **2000**, *39*, 365–366.
- (38) Jardin, C.; Oeckler, O.; Mattausch, H. J.; Simon, A.; Halet, J. F.; Saillard, J. Y.; Bauer, J. *Z. Anorg. Allg. Chem.* **2001**, *627*, 1389–1394.
- (39) Jardin, C.; Oeckler, O.; Mattausch, H. J.; Simon, A.; Halet, J. F.; Saillard, J. Y.; Bauer, J. *Inorg. Chem.* **2000**, *39*, 5895–5900.
- (40) Lassoued, S.; Gautier, R.; Boutarfaia, A.; Halet, J. F. *J. Organomet. Chem.* **2010**, *695*, 987–993.
- (41) Renaudin, G.; Dieudonne, B.; Avignant, D.; Mapemba, E.; El-Ghozzi, M.; Fleutot, S.; Martinez, H.; Cerny, R.; Dubois, M. *Inorg. Chem.* **2010**, *49*, 686–694.
- (42) Beche, E.; Charvin, P.; Perarnau, D.; Abanades, S.; Flamant, G. *Surf. Interface Anal.* **2008**, *40*, 264–267.
- (43) Goremychkin, E. A.; Osborn, R.; Sashin, I. L.; Riseborough, P.; Rainford, B. D.; Adroja, D. T.; Lawrence, J. M. *Phys. Rev. Lett.* **2010**, *104*, 176402.
- (44) West, A. R. *Basic Solid State Chemistry*, 2nd ed.; John Wiley & Sons, Ltd.: Chichester, West Sussex, England, 1999.
- (45) Schmitt, R.; Blaschkowski, B.; Eichele, K.; Meyer, H. J. *Inorg. Chem.* **2006**, *45*, 3067–3073.

- (46) Zogal, O. J.; Florian, P.; Massiot, D.; Paluch, S.; Shitsevalova, N.; Borshchovsky, D. F. *Solid State Commun.* **2009**, *149*, 693–696.
- (47) (a) Han, M. K.; Morosan, E.; Canfield, P. C.; Miller, G. J. Z. *Kristallogr.* **2005**, *220*, 95–101. (b) Gout, D.; Benbow, E.; Gourdon, O.; Miller, G. J. *J. Solid State Chem.* **2003**, *176*, 538–548.
- (48) Kittel, C. *Introduction to Solid State Physics*, 6th ed.; John Wiley & Sons, Inc.: New York, 1986.
- (49) Palstra, T. T. M.; Nieuwenhuys, G. J.; Mydosh, J. A.; Buschow, K. H. J. *Phys. Rev. B* **1985**, *31*, 4622–4632.
- (50) Blanchard, P. E. R.; Cavell, R. G.; Mar, A. J. *Solid State Chem.* **2010**, *183*, 1477–1483.